applied sciences

MDPI

Article

An Improved Abrasive Flow Processing Method for Complex Geometric Surfaces of Titanium Alloy Artificial Joints

Li Zhang, Zhimin Yuan, Dapeng Tan * and Yi Huang

Key Lab of E&M, Ministry of Education & Zhejiang Province, Zhejiang University of Technology, Hangzhou 310014, China; zhangli@zjut.edu.cn (L.Z.); 18868831729@163.com (Z.Y.); huangyi1999@zjut.edu.cn (Y.H.)

* Correspondence: tandapeng@zjut.edu.cn; Tel.: +86-571-8832-0831

Received: 25 May 2018; Accepted: 24 June 2018; Published: 25 June 2018

Featured Application: A new material removal theoretical model of abrasive flow is set up, and it can offer solution scheme of fluid-based precise processing for workpieces with irregular geometric structures. An improved abrasive flow processing method is proposed to provide direct technical supports for the manufacturing of titanium alloy artificial joints.

Abstract: Precise processing for complex geometric surfaces of titanium alloy artificial joints has higher technical difficulties. This paper addresses the matter by proposing an improved abrasive flow processing method. According to the micro-cutting principle, the processing mechanism on curvature surface of the titanium alloy workpiece by the abrasive flow is analyzed. A new material removal model of abrasive flow is proposed to reveal the processing regularities for complex geometric surfaces of titanium alloy artificial joints. Based on the model, in combination with the realizable k-ε turbulence model, the total force affecting on a wall region of constrained flow passage is obtained to estimate the quantity of material removal. A multi-segment profiling constrained flow passage is designed, and an optimized flow passage scheme is provided. Numerical results show that the optimized flow passage can improve the pressure/velocity profile uniformities of abrasive particles; by the product of velocity and pressure, the cutting coefficient for complex surface is obtained. A processing experimental platform is developed, and the processing experiment results indicate that the proposed material removal model can estimate the processing effects and removal regularities, and the size accuracy and surface quality of the titanium alloy surface are improved.

Keywords: abrasive flow; complex surface; titanium alloy artificial joint; material removal model; multi-segment profiling flow passage

1. Introduction

Titanium alloy materials have been widely used in many engineering areas, especially for the artificial joints manufacturing, because of their high specific strength, good corrosion resistance and excellent biocompatibility [1–6]. However, the manufacturing technologies of titanium alloy artificial joints face two challenges. Firstly, titanium alloy has poor thermal conductivity and low modulus of elasticity, so the adhesion wear between finished surface and cutting tool reduces machining efficiency. Secondly, traditional cutting tools can hardly adapt the complex surfaces of artificial joints (shown in Figure 1), and easily conduct processing trails to cause negative influences of surface roughness and uniformity [7–10].

Related research works suggested that abrasive flow processing is an effective approach for the manufacturing of workpiece with complex geometric surfaces [11–13]. Based on the high viscoelasticity

fluid media, considering the normal force and number of abrasive particles, Dong et al. set up a material removal rate model [14]. To resolve the matter of small-scale geometric surfaces for mold manufacturing, Ji et al. presented a fluid-based precision processing approach by the low-viscosity softness abrasive flow (SAF). By using a constrained module on the machined workpiece, an enclosed constrained flow passage is formed. According to the particle–wall collusion effects, the micro-force/cutting for irregular geometric surfaces can be performed. Based on the pressure/velocity coefficients in Preston equation, the technical procedures of SAF processing are confirmed, and the material removal empirical formula can be acquired [15–18]. Williams and Rajurkar proposed a metal material removal model of abrasive flow processing to estimate the number of particles participating in the cutting [19]. Rajendra set up a model for material cutting and surface texture of fluid-based processing, and computed the tangential force on machined surface to explore the effect of normal force on the energy consumption [20]. Jain et al. studied the cutting energy and cutting force of abrasive flow processing, and analyzed the contacting effects of the normal cutting force and the particle number [21]. By the abrasive flow processing for gears, Yan et al. found that particles cutting action in the restriction section is effective [22]. Wang and Duan used the rheology to describe the processing mechanism of two-phase abrasive flow. Their results showed that the processing capacity is determined by the cutting force containing shear stress and normal stress [23]. Tang et al. analyzed the pressure characteristics on the machined surface roughness in abrasive flow processing, and found that the tangential force is an important influence factor to processing efficiency [24].

Abrasive flow is a two-phase viscous medium composed of continuous fluid phase and discrete solid phase, and the movement of solid particle is the key matter for the processing ability. The interaction mechanism between mass, momentum and energy of two-phase abrasive flow is a nonlinear fluid mechanic issue [25–28]. If the particle volume fraction is small enough (less than 15%), the discrete phase model (DPM) can be used to describe the discrete solid phase [29]. The volume of fluid (VOF) is used to track the dynamical variations of phase interfaces, and also to simulate the matters of laminar flow, breaking of liquid jet, the movement of big bubbles in water, free surface flow, etc. [30]. Level-set method (LSM) is a numerical technique for tracking and modeling of phase interface topological structure. It can solve the phase field transition process of abrasive flow in the constrained flow passage [31]. Yuan et al. used the Euler model to analyze the low-Reynolds-number flow field profiles in an enclosed physical space [32]. Zhang et al. used the SAF to process titanium alloy artificial joints (shown in Figure 1), and then found that fluid resistance is caused by path losses, local losses and uneven profiles of velocity and dynamic pressure of abrasive flow field. The above factors would result in uneven processing effects and lower efficiency [1,33].

Figure 1. Titanium alloy artificial joints with complex geometric surfaces [1].

To address the technical problems of precision processing for titanium alloy artificial joints, this paper proposes an improved abrasive flow processing method for complex geometric surfaces. By the multi-segment profiling constraint modules, a circular constrained flow passage that can cover the machined curvature surface is constructed. Consequently, the machined surface becomes a part of the wall flow passage. If the abrasive flow is under the full-developed turbulence state, the micro-cutting effects are conducted by the disorder movement of abrasive particles, and the processing chippings will be carried off by the abrasive flow.

Based on the contacting kinematics regularities between particles and machined surface, this paper mainly studies the tangential velocity distribution of particles in abrasive flow, and the particle pressure to machined surface in the cutting process. For the processing mechanism of abrasive flow, the normal grinding force, particle movement and cutting depth coefficient are researched, and a new material removal model of abrasive flow is set up. Based on the above model, in combination with the realizable k-ε turbulence model, the total force affecting on a wall region of constrained flow passage is obtained to estimate the quantity of material removal, and to provide technical supports for the regulation of abrasive flow processing.

2. Multi-Segment Profiling Constrained Flow Passage

In this study, the abrasive flow consists of distilled water, electrostatic dispersant and silicon carbide particles. It is a kind of processing medium with low abrasive particle fraction and high motion velocity, and the abrasive particle fraction is generally less than 15%. Abrasive flow is a typical two-phase incompressible fluid, in which the distilled water is the carrier of abrasive particles, and the electrostatic dispersant can address the even particle distribution of abrasive flow [34–39].

To adapt the complex surface of artificial joint, a multi-segment profiling constrained flow passage is designed, as shown in Figure 2. The machined workpiece is a simplified artificial knee joint. There are seven segments of constrained modules covering the curvature surface of the workpiece. Accordingly, a circular constrained flow passage is formed, in which the machined surface is the lower wall of the flow passage. Firstly, the abrasive flow is driven by a diaphragm pump with the required inlet conditions. Then, the abrasive flow enters the profiling constrained flow passage and forms full-developed turbulence state. The micro-force/cutting is performed by the random motion of abrasive particles driven by the turbulence. Finally, it flows out with the processing chippings from the outlet, and forms a processing cycle.

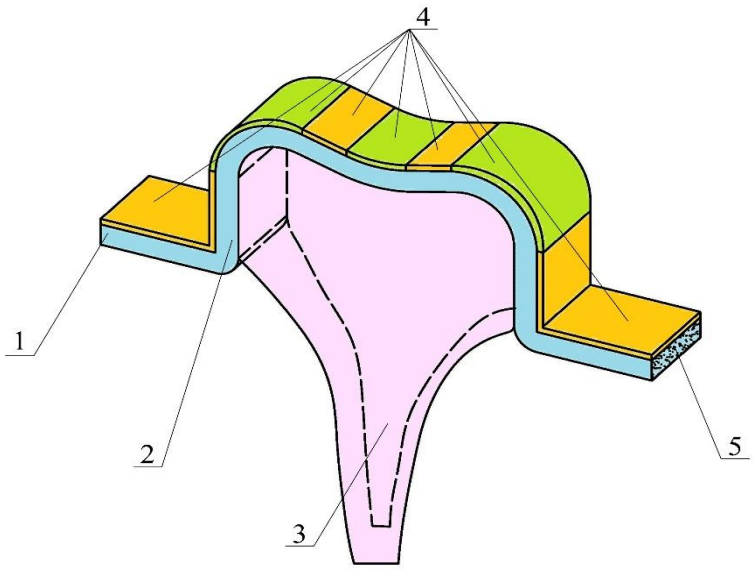

Figure 2. Structural diagram of constrained flow passage for complex surface of artificial joint: 1, inlet; 2, constrained flow passage; 3, workpiece; 4, constrained module (seven segments); 5, outlet.

3. Material Removal Model of Abrasive Flow

3.1. Normal Grinding Force of Abrasive Particle

Since the particles have no certain geometric shape, a particle model is commonly set up with conicalness and pyramid. In this paper, the silicon carbide particle is taken as the abrasive particle, and is set as a regular hexahedron model [40–42].

As presented in Section 2, the abrasive flow enters the constrained flow passage and forms the fully-developed turbulent state. For the movement complexity of turbulence, we select a single abrasive particle in contact with complex surface as the study subject, in which the normal grinding force is a key parameter. Based on the above hypothesis, the material removal model of single particle can be described by Figure 3.

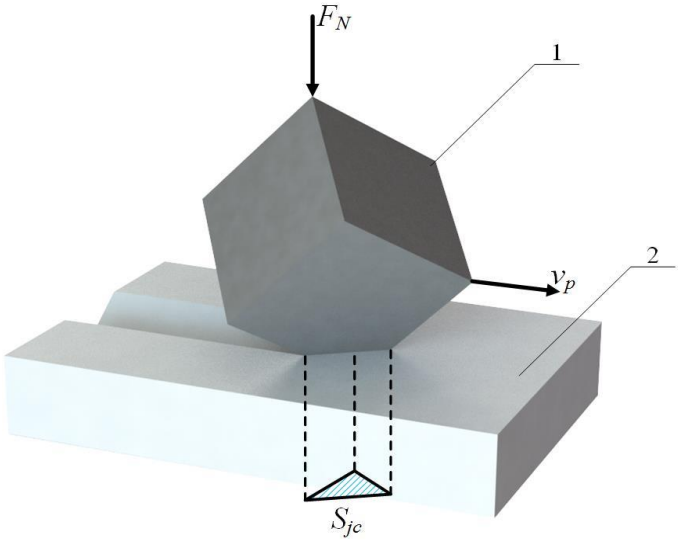

Figure 3. Material removal model of single particle: 1, particle; 2, machined surface.

In this model, abrasive flow is turbulent so that the abrasive particles in the flow passage strike and cut the complex surface under the effect of normal force in vertical direction, where F_N is the pressure of fluid driving particle. The cutting force of the single abrasive particle can be expressed by [43–45]:

$$F_n = c_n p S_{jc} \tag{1}$$

where c_n is a constant of particle wearing, and determined by the particle shape and granulate hardness; p is the average normal stress of particles collide with surface; and S_{jc} is the projection of abrasive particle on the machined surface and can be described as

$$S_{jc} = \sqrt{\frac{2F_N}{3\sqrt{3}H}} \tag{2}$$

where H is surface hardness of workpiece. Therefore, the indentation depth is determined by the normal force and the hardness of workpiece.

The projection area is supposed to be an isosceles right triangle, and the waist length is given by

$$a_y = \sqrt{\frac{4F_N}{\sqrt{3}H}} \tag{3}$$

According to micro-cutting wear mechanism [46–48], a small part of the abrasive particle is pressed into the machining surface by the normal force. Then, an abrasive particle is driven by the friction between the base fluid and abrasive particle. The furrow action is taken by abrasive particle on the machined surface, so the wear scars with trough shapes are appeared on the surface. For the turbulent abrasive flow processing, high accuracy finishing process is achieved by numerous irregular wear scars with trough shapes. In this research, the material of abrasive particle is silicon carbide, and the material of workpiece is titanium alloy. Because the hardness of silicon carbide is greater than the hardness of titanium alloy, the processing result is affected by the hardness of silicon carbide. If the slip distance of a particle is ds, the removal volume of different machined surface is described as:

$$dV = \begin{cases} \frac{F_n}{2\sqrt{H}} \cdot \frac{3R+\delta}{3R+3\delta-3a_y} ds, \text{ concave surface} \\ \frac{F_n}{2\sqrt{H}} ds, \text{ plane} \\ \frac{F_n}{2\sqrt{H}} \cdot \frac{3R-\delta}{3R-3\delta+3a_y} ds, \text{ convex surface} \end{cases} \quad (4)$$

If the removal volume is maximum, the machined surface is with concave profile. Similarly, if the workpiece has a convex surface, the removal volume is minimum.

3.2. Abrasive Particle Movement in Abrasive Flow Processing

Abrasive flow is a wear particle group made up of many abrasive particles, so the average number of abrasive particles follows a certain law of mathematical statistics. This paper supposes that there is a random particle distribution in the constrained flow passage, as shown in Figure 4.

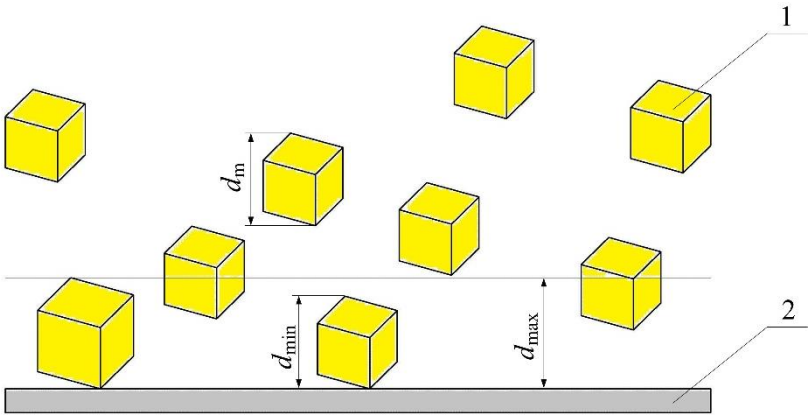

Figure 4. Distribution of abrasive particles in abrasive flow: 1, particles; 2, workpiece.

This paper supposes that abrasive particles in the abrasive flow are evenly distributed, and the sizes of abrasive particles accord with the Gaussian distribution. In the volume whose floor space is a unit area with height $d_{\max}$, the number of abrasive particles is described as:

$$N_0 = \frac{6}{\pi} \cdot \frac{\psi_a}{1+\psi_a} \cdot \frac{\rho_{\text{mix}}}{\rho_{\text{sic}}} \cdot \frac{d_{\max}}{d_a^3} \quad (5)$$

where ρ_{mix} is the density of the abrasive flow; ρ_{sic} is the density of the abrasive particle; $d_{\max}$ is the maximum diameter of abrasive particle; and d_a is average diameter of abrasive particle.

Since the geometric sizes and central locations of abrasive particles in abrasive flow are random, they are supposed to obey probability distribution. If the particle number for cutting and the particle number in boundary layer of workpiece surface are not equal, the abrasive particles contact surface in

the fluid layer with height d_{max}. The share of abrasive particles participating in cutting is supposed as k_a, so the number of affecting abrasive particles is N_a [49,50], as expressed by Equation (6):

$$N_a = k_a N_0 \tag{6}$$

where k_a is a probability function related to the diameter and distribution of abrasive particles, and $k_a < 1$.

3.3. Material Removal Model in Contact Length

The material removal depth in per contact length is defined as removal depth of workpiece surface contacting with abrasive particle, and known as linear removal rate [51–53]. As shown in Figure 5, an element of abrasive flow is cut out of boundary layer on the workpiece surface, in which dx, dy, and dz are the width, height and length, respectively. Because different positions have different curvatures, there is no a certain worn volume in the abrasive flow processing.

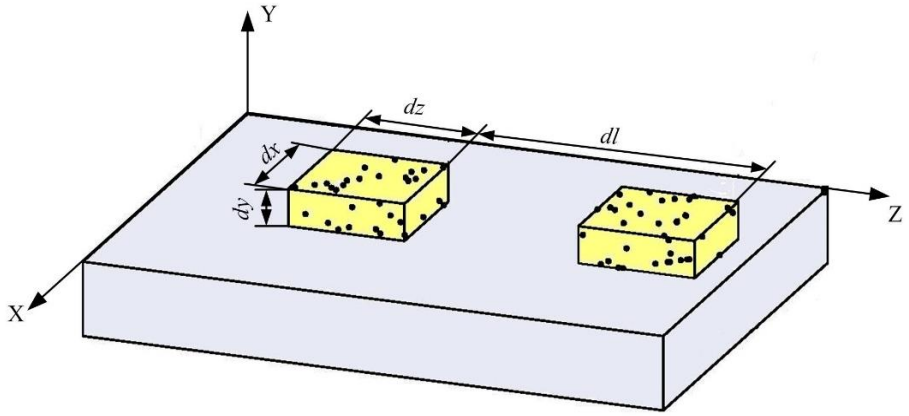

Figure 5. Diagram of material removal model of abrasive flow processing: 1, abrasive flow micro-body; 2, workpiece.

Cutting depth of abrasive particle is less than pressed depth on the workpiece surface during processing [54]. For the cutting process, the number of abrasive particles is very great, so the remove depth cannot simply be expressed by cutting depth. When many abrasive particles participate in cutting, the cutting depth will have an average distribution. In the model in Figure 4, dy is the cutting depth of abrasive flow. Consequently, referring to Equation (6), the number of abrasive particles in the area $dxdz$ of micro-element is approximately $dxdzN_a$. When a micro-element flows from z_0 to $z_0 + ds$, the normal pressure F_n of the abrasive flow on the abrasive particle is a certain value. According to micro-cutting wear mechanism, the material removal depth is described by:

$$D_l = \frac{dy}{dz} = N_a \cdot \frac{K}{K_v} \cdot \frac{F_n}{H} \tag{7}$$

where K_v is the material removal coefficient. Therefore, the nonlinear material removal amount is proportional to the force of abrasive flow on the particle, and is related to the curvature of workpiece surface.

3.4. Cutting Depth Coefficient of Abrasive Flow Processing

According to the load analysis of single abrasive particle and the statistic distribution of abrasive particle in the flow passage, a material removal model of abrasive flow processing is proposed. For the

material removal depth model of high viscoelastic abrasive flow, this paper defines a cutting depth coefficient for the curvature variations of different workpiece surface:

$$K_0 = \begin{cases} \frac{N_a K c_n S_{jc} H_p}{K_{dv} H} \cdot \frac{3R+\delta}{3R+3\delta-3a_y} ds, \text{ concave surface} \\ \frac{N_a K c_n S_{jc} H_p}{K_{dv} H} ds, \text{ plane} \\ \frac{N_a K c_n S_{jc} H_p}{K_{dv} H} \cdot \frac{3R-\delta}{3R-3\delta+3a_y} ds, \text{ convex surface} \end{cases} \quad (8)$$

where the factors impacting on the coefficient of cutting depth are as follows: (1) surface hardness; (2) surface curvature; (3) surface roughness; (4) particle granularity; (5) particle mass fraction; (6) particle shape; and (7) turbulence intensity in flow passage.

According to Equation (8), the equation of the material removal depth in unit time is:

$$d = K_0 p v_1 \quad (9)$$

It is the material removal model of turbulent abrasive flow processing for complex surface. Apparently, Equation (9) is similar to Preston equation [55]. For the determination of the material removal coefficient of different machined surface, the distributions of the particle velocity and particle pressure to machined surface should be optimized to get a uniform flow field.

4. Fluid Dynamic Model of Abrasive Flow

4.1. Turbulence Model

As presented in Section 1, abrasive flow is a typical two-phase engineering fluid media, and with the characteristics of high velocity, weak viscosity and turbulent state [56]. Based on the above characteristics of abrasive flow, the particle group is supposed as a pseudo-fluid interpenetrated with fluid.

Standard *k*-ε model is a commonly used classical turbulence model, but it will be distorted for the strongly swirling flow, curved wall flow and curving streamline flow. In the constrained flow passage, it could result in negative normal stresses. Different from the standard *k*-ε turbulence model, the expression for the turbulent viscidity in realizable *k*-ε model introduces rotation and curvature, so it will be able to adapt to avoid the negative normal stress [57–59]. Accordingly, a fluid dynamic model for abrasive flow processing is set up based on the realizable *k*-ε turbulence model. Based on the model, the profiles of pressure and velocity of abrasive flow on the workpiece surface are obtained, and the optimized processing conditions and constrained modules could be confirmed.

In the realizable *k*-ε turbulence model, the transport formulae for turbulent kinetic energy k and dissipation rating ε are described as:

$$\frac{\partial(\rho k)}{\partial t} + \frac{\partial(\rho k u_i)}{\partial x_i} = \frac{\partial}{\partial x_j}\left[\left(\mu_1 + \frac{\mu_t}{\sigma_k}\right)\frac{\partial \varepsilon}{\partial x_j}\right] + G_k - \rho\varepsilon \quad (10)$$

$$\frac{\partial(\rho \varepsilon)}{\partial t} + \frac{\partial(\rho \varepsilon u_i)}{\partial x_i} = \frac{\partial}{\partial x_j}\left[\left(\mu_1 + \frac{\mu_t}{\sigma_\varepsilon}\right)\frac{\partial \varepsilon}{\partial x_j}\right] + \rho C_1 E \varepsilon - \rho C_2 \frac{\varepsilon^2}{k + \sqrt{v\varepsilon}} \quad (11)$$

where ρ is fluid density; x_i and x_j are coordinate components; σ_k and σ_ε are turbulent Prandtl numbers of turbulent kinetic energy k and dissipation rate ε; G_k is turbulent kinetic energy resulted from average velocity gradient; μ_1 is molecular viscosity coefficient; and μ_t is turbulence viscosity coefficient. σ_k = 1.0, σ_ε = 1.2, and C_2 = 1.9 [60–62].

4.2. Dynamic Characteristics of Abrasive Flow Processing

Based on the above hypothesis, the total force affecting on a wall region of constrained flow passage can be regarded as the dot product of the components of pressure and viscous force, and can be described as:

$$F_a = \mathbf{a} \cdot \mathbf{F}_p + \mathbf{a} \cdot \mathbf{F}_v \tag{12}$$

where $\mathbf{a}$, $\mathbf{F}_p$, and $\mathbf{F}_v$ are the force vector, pressure vector and viscous vector, respectively [63].

Considering the actual physical parameters of abrasive flow field, the related force coefficients can be obtained for the target wall regions, by the reference values of velocity, pressure, viscosity and turbulent kinetic energy. Generally, the force coefficient can be expressed by $0.5\rho v^2 S$, in which ρ is the fluid density, v is the fluid velocity, and S is the contacting area. Accordingly, the force parameters of abrasive flow in constrained flow passage for different target wall regions can be acquired.

For a fluid micro-element of abrasive flow, the total moment vector of a wall contacting area can be expressed by the cross product of the components of pressure and viscous force, i.e., a vector generated by the moment center A to the force origin B, as shown in Figure 6, and the expression of total moment vector can be described as:

$$\mathbf{M}_A = \mathbf{r}_{AB} \times \mathbf{F}_p + \mathbf{r}_{AB} \times \mathbf{F}_v \tag{13}$$

where A is the moment center of a wall contacting area in flow passage; B is the force origin a fluid micro-element of abrasive flow; $\mathbf{r}_{AB}$ is the fluid micro-element moment vector; and $\mathbf{F}_p$ and $\mathbf{F}_v$ are the force components of pressure and viscous force, respectively.

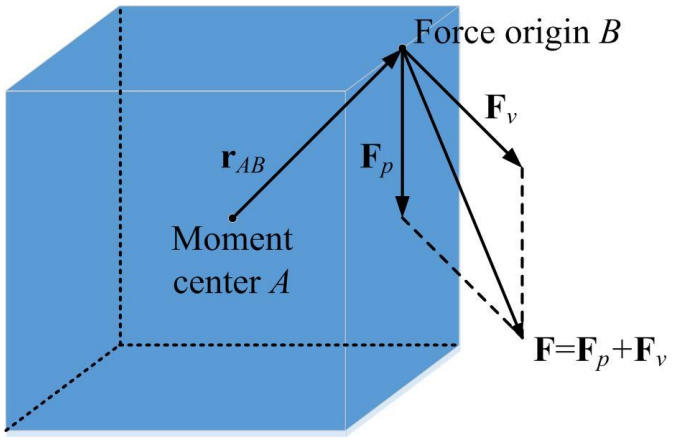

Figure 6. Moment vector of a fluid micro-element of abrasive flow.

According to the above reduction, the moment vector direction can be determined by the right-hand rule. Similar to the force vector, by the actual physical parameters of abrasive flow field, the corresponding moment coefficients can be obtained for the target wall regions, by the reference values of velocity, pressure, viscosity and turbulent kinetic energy. Therefore, the moment coefficient can be expressed by $0.5\rho v^2 SL$, in which L is the fluid affecting length in constrained flow passage. Consequently, the total moment and related coefficients of abrasive flow in constrained flow passage for different target wall regions can be obtained.

By this computation method, according to fundamental physical parameters, force vector, moment vector and coefficients of abrasive flow field, all moments of the target wall region about different coordinate axes can be obtained, i.e., the dot product between a unit vector and the related axis direction. Subsequently,

to restrict the rounding error, a reference pressure variable is adopted to normalize the pressure of abrasive flow micro-element, i.e., the pressure vector sum on the affecting interface:

$$\mathbf{F}_p = \sum_{i=1}^{n} \left(p - p_{ref}\right) S\hat{n} \tag{14}$$

$$\mathbf{F}_p = \sum_{i=1}^{n} pS\hat{n} - p_{ref} \sum_{i=1}^{n} S\hat{n} \tag{15}$$

where n is the interface number of abrasive flow micro-element, S is the affecting area on the interface, and $\hat{n}$ is the unit normal to the interface.

For the 2D flow field in constrained flow passage, the stress components of pressure and viscous force can be regarded as the line distribution, in which crossing point of the line and reference line is the pressure center point. Apparently, there is a zero moment on this point. Considering a 3D flow field, the stress components of pressure and viscous force can be described as the spatial force system in a fluid micro-element. In this hypothesis, the resultant moment is described as

$$M_x = F_z Y - F_y Z \tag{16}$$

$$M_y = F_x Y - F_z Z \tag{17}$$

$$M_z = F_y Y - F_x Z \tag{18}$$

In the 3D flow flied system, we can define a reference plane for the target wall region, and make the two equations in Equations (16)–(18) be zero. Then, the crossing point of the axis and reference plane about the target wall region can be obtained. For a 2D instance, only Equation (18) should be considered by the user-specified reference line to determine the center of pressure.

5. Numerical Simulation and Results Discussion

5.1. Numerical Model and Grid Meshing

The profiling constrained flow passage for titanium alloy complex surface of artificial joint is composed of multi-segment constrained modules and workpiece surface, and the numerical model is shown as Figure 7. Firstly, a three-dimensional mechanical structure model is set up, and then it is imported into a finite element model. The radius of circular arc of upper surface from left to right are 10 mm, 32 mm, and 10 mm, respectively. The mesh dividing is completed and essential boundary condition is configured, in which the element is Tet/Hybrid, the type is TGrid, the interval size is 1, and the number of cells is 324,041. The mesh dividing schematic of the profiling constrained flow passage is shown in Figure 7b. For the essential boundary condition setting, the inlet is VELOCITY_INLET, the outlet is OUTFLOW, and other sides is WALL.

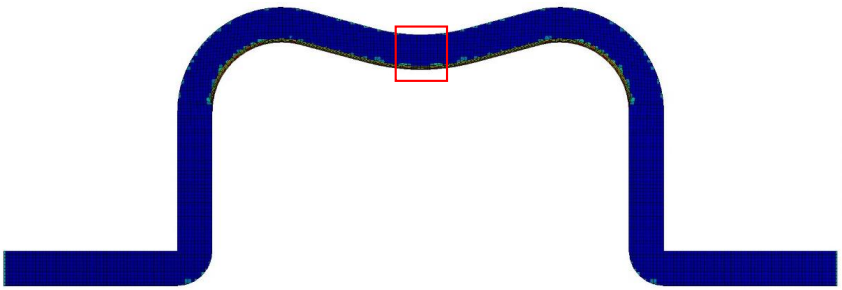

(**a**)

Figure 7. *Cont.*

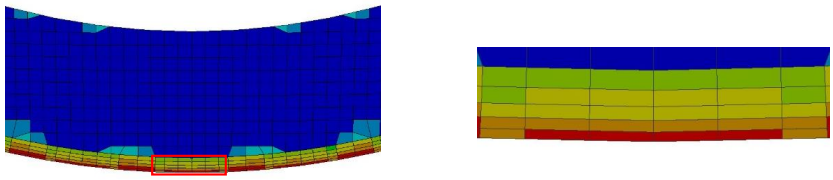

(**b**) (**c**)

Figure 7. Numerical model of profiling constrained flow passage for titanium alloy complex surface: (**a**) orthogonal view; (**b**) local enlarged view; and (**c**) local enlarged view of a region.

This paper selects 3D single-precision steady implicitly pressure solver, and the solution is obtained by the SIMPLEC algorithm of pressure-linked equations. In this paper, the solid particle phase is silicon carbide particle, the density is 3170, the mean diameter of abrasive particle is 0.05 mm, and the volume fraction is 0.1; the fluid phase is distilled water. According to computed Reynolds number, the abrasive flow in the flow passage can form the turbulent state, and the turbulence intensity is 9.8%. Based on the features of flow passage, the solving conditions are configured for the Euler model and realizable *k*-*ε* turbulence model.

5.2. Numerical Results Discussion

Figure 8 shows that the surface of workpiece is composed of three different arcs. There are several poles and inflection points. Oscillations and fluctuations of energy in the fluid flow have a direct relevancy to the shape of workpiece. According to the structure of multi-segment constrained modules, the profiling constrained flow passage can be divided into five regions: the radius of L1 (X range: 0–0.01259 m) is 0.01 m; L2 (X range: 0.01259–0.02224 m) is a plane; the radius of L3 (X range: 0.02224–0.03649 m) is 0.03 m; L4 (X range: 0.03649–0.04535 m) is a plane; and the radius of L5 (X range: 0.04535–0.06 m) is 0.01 m. For optimizing the constrained flow passage, the velocities of particles and the contact forces between particles and workpiece are analyzed by the computational fluid dynamics (CFD) method. The distance between the observation plane and workpiece is set as 0.005 mm, and principal parameters are listed in Table 1.

Table 1. Physical parameters of abrasive flow.

Velocity/m·s^{-1}	Dynamic Viscosity/(Pa·s)	Particle	Volume Fraction/%	Hydraulic Diameter/m	Length *l*/m
10	2.06	SiC	10	0.008	0.06

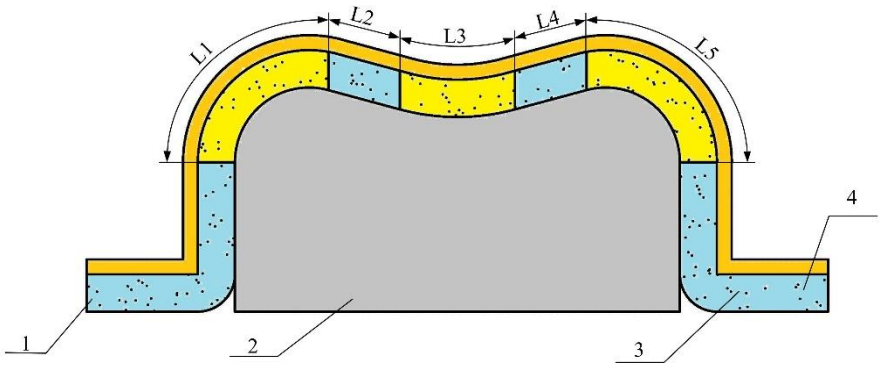

Figure 8. Division of curvature region: 1, inlet; 2, workpiece; 3, constrained flow passage; 4, outlet.

Velocities of particles in profiling constrained flow passage are shown in Figure 9. In Figure 9a, the X velocities in the L1 and L5 are close to 0. Figure 9b shows that the Y velocities in the L1 are obviously decreased, but the Y velocities in L5 are obviously increased. Because particles vertically enter L1 and leave L5, the X velocities in L1 and L5 are close to 0. Due to the particles moving parallel to the workpiece along with fluid after particles enter L1, the included angle between vectors of particles and vertical direction becomes larger, and the Y velocities in L1 are decreased. The velocity variation in L5 is similar. The X velocities of particles in L2, L3 and L4 are the same, but Y velocities of particles in L2, L3 and L4 are changed slowly. From the flow field profile results, we can conclude the following laws. (a) On the different machined surface, velocities direction of particles participating in cutting are changed. In the plane, the X velocities and Y velocities of particles are not change nearly. (b) On the curved surface, the amplitudes of X velocities and Y velocities are changed with the radius of the curved surface.

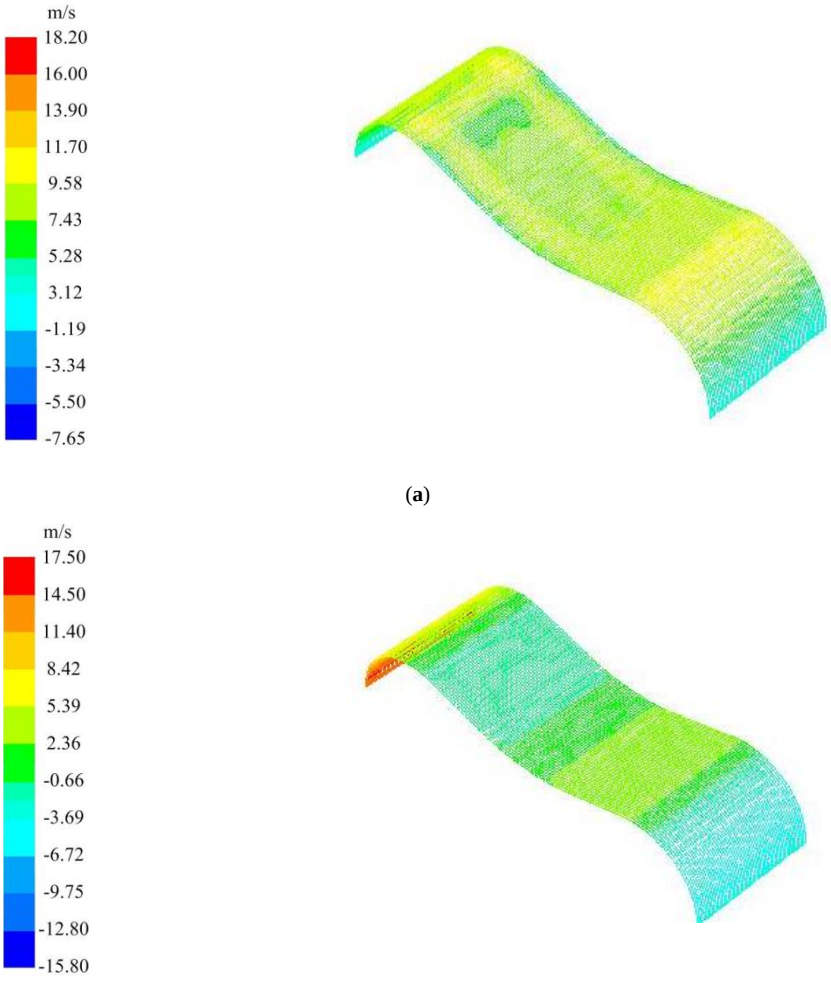

Figure 9. Velocity vectors of particles: (**a**) X velocities of particles; and (**b**) Y velocities of particles.

The X/Y velocities of particles can be obtained by CFD method, but the tangential velocity must be obtained by calculation for further study, as shown in Figure 10. The trend of the tangential velocity in L1 and L5 is similar to the Y velocity, and the maximum in L1 is bigger than in L5. In L2, the tangential velocity is gradually decreased, but, in L4, the tangential velocity is gradually decreased and the changing speed is smaller. In L3, the tangential velocity is gradually increased. On the curved surface, the bigger the radius of the curved surface is, the more quickly the velocity of the particle changes.

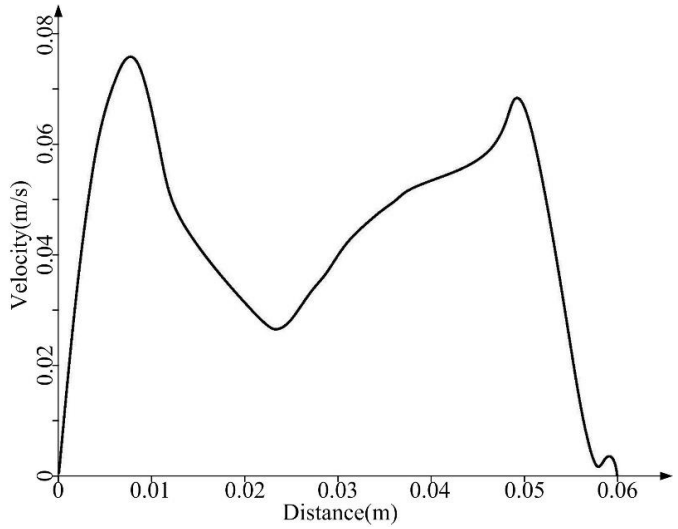

Figure 10. Tangential velocity profile in constrained flow passage.

Based on the numerical simulation results of the tangential velocity, the following regularities can be acquired. Because of the linear loss, the tangential velocity is gradually decreased. On the impact face, the tangential velocity is gradually increased, but, on the non-impact face, the tangential velocity is gradually decreased, and the changing speed is much bigger than the changing speed caused by the linear loss.

To obtain the affecting forces of particles on the workpiece, L1 and L5 are evenly divided into 14 planes, respectively. L3 is evenly divided into 12 planes. The X forces and Y forces of particles on the planes is obtained by the CFD method, and the total pressure force is shown in Figure 11. The forces of particles in L1 are obviously reduced; the forces of particles in L2 are almost as much as in L3; the forces of particles in L4 are much higher than in L2 and L3; the minimum forces of particles in L5 are on the right of L5 and they gradually become larger; the forces on the left of L1 are much higher than on the right of L5, and forces in L2 are much smaller than in L4; the force peaks in L1 and L5 and the low of L3 are almost equal. Because L2 and L4 are plane, the forces in L2 and L4 are bigger than in the peaks of L1, L5 and L3.

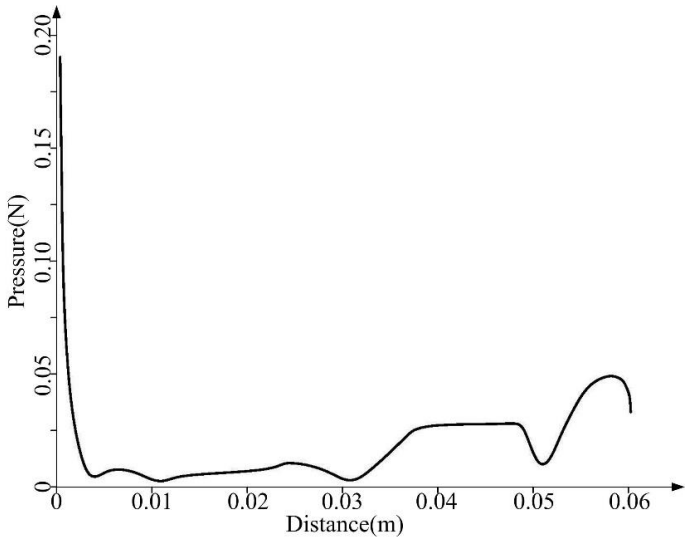

Figure 11. Pressure profile of particles on the workpiece.

Referring to the simulation results of pressure, the following laws can be obtained. The normal force of particle to the impact surface is higher than the non-impact surface. On the curved surface, the normal force of particle is changed, and the bigger the radius of the curved surface is, the more quickly the velocity of the particle changes. Based on Equation (9), a PV product graph is made to study the cutting depth coefficient K_0, as shown in Figure 12. The products in L2, the left of L3, the right of L3 and L4 and the middle of L5 are higher than other areas. According to the numerical results of PV graph, the product variation regularities of force and velocity can be obtained. Consequently, an optimized constrained flow passage is designed, as shown in Figure 13.

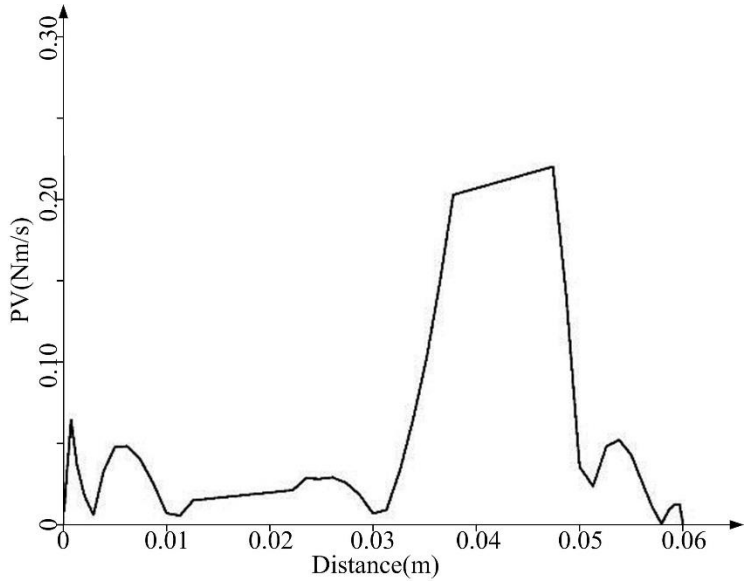

Figure 12. The product of force and velocity.

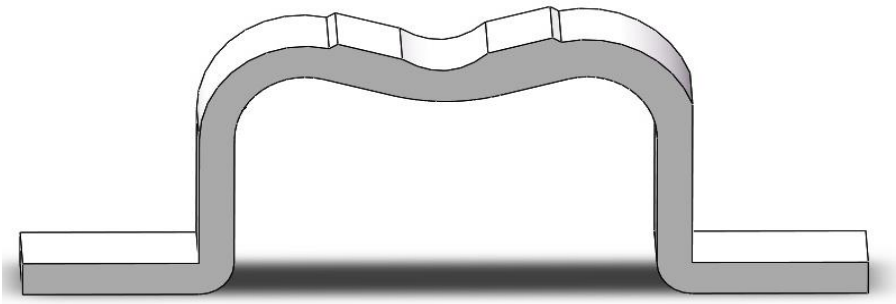

Figure 13. The Optimized constrained flow passage.

The velocities of particles in the optimized constrained flow passage are shown in Figure 14, and the tangential amplitude profile is shown in Figure 15. In Figure 14, we can find that the velocities in L1 and L5 of particles in the optimized constrained flow passage are similar to the velocity of particles in the original flow passage; the velocities in L2, L3 and L4 of the optimized constrained flow passage are more uniform than the velocities in the original flow passage.

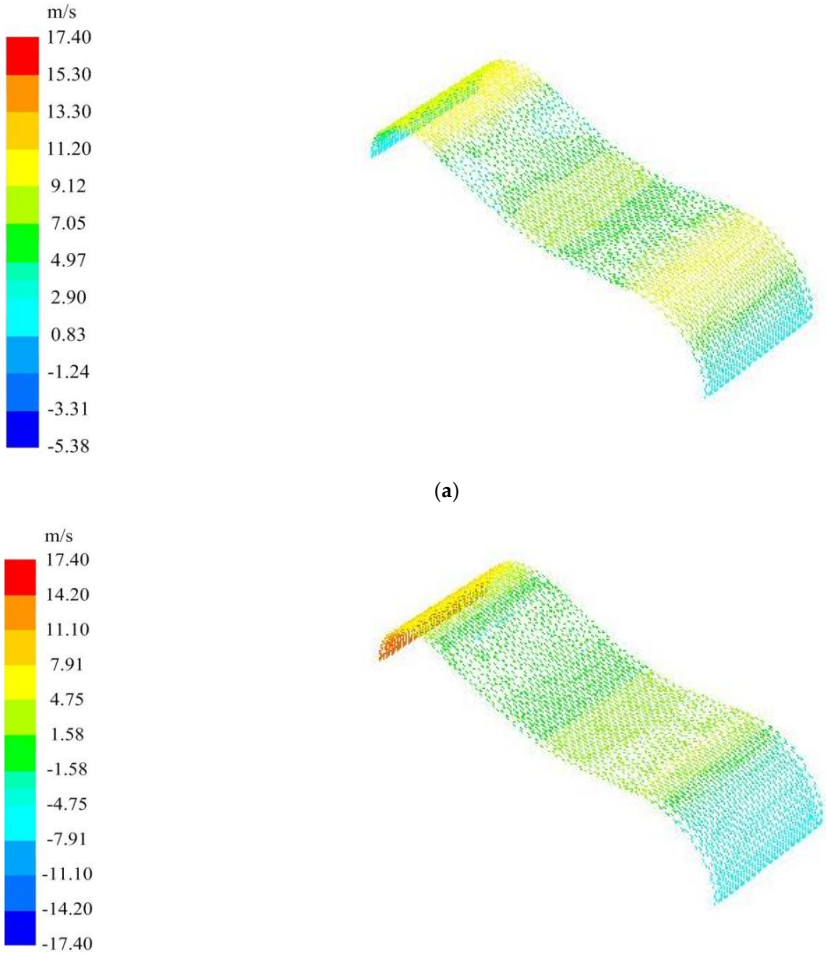

Figure 14. Velocity vectors of particles in the optimized flow passage: (**a**) X velocities of particles; and (**b**) Y velocities of particles.

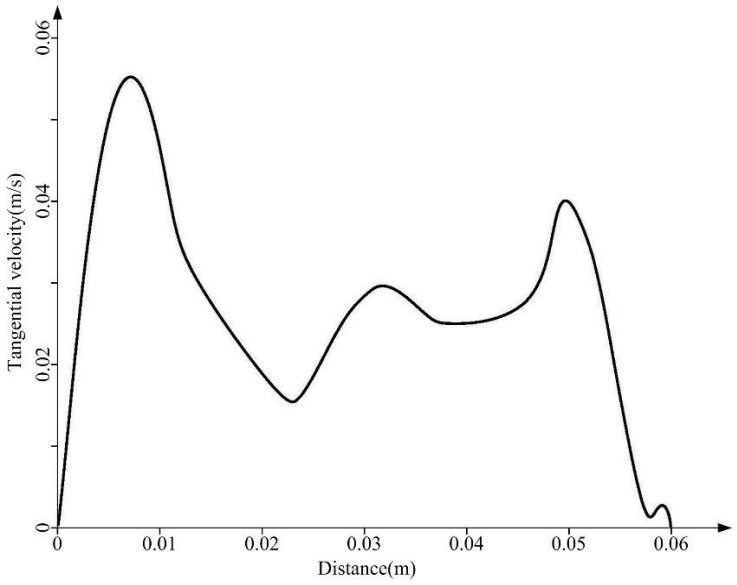

Figure 15. Tangential velocity of particles in the optimized flow passage.

The forces of particles in the optimized flow passage are shown in Figure 16. The product profile of forced and velocity of particles in the optimized flow passage is shown in Figure 17. Figure 16 shows that the forces graph is more chaotic than the forces graph of the original flow passage, but Figure 17 shows that the PV graph is much smoother than the PV graph of the original flow passage. In consideration of precision finishing, the removal volumes in all area of workpiece should be almost equal, so the optimized flow passage is more applicable for precision finishing for complex surface.

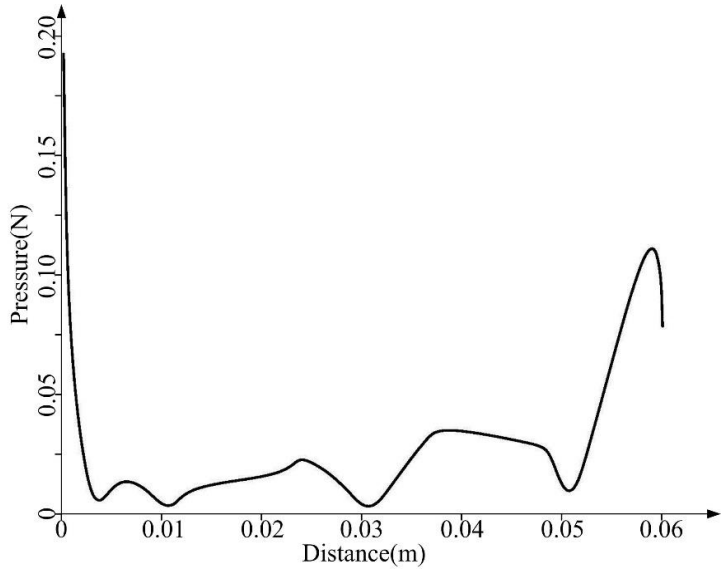

Figure 16. Forces of particles in the optimized flow passage.

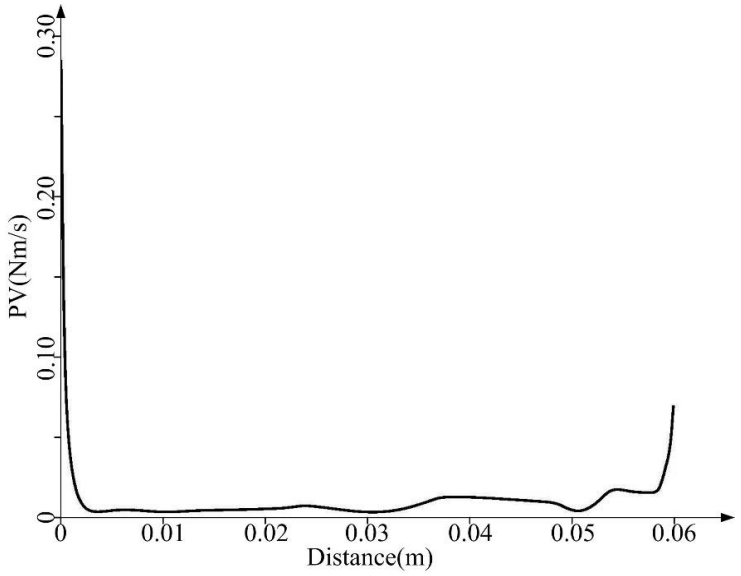

Figure 17. The product of forced and velocity of particles in the optimized flow passage.

According to the cutting depth coefficient and the curve of PV, the theoretical cutting coefficients of different position in the optimized constrained flow passage can be calculated. Because processing conditions of abrasive flow processing are very complicated, the accurate theoretical cutting coefficients are hard to calculate. Therefore, the theoretical cutting coefficients of plane (L2 and L4) are set as 1, and theoretical cutting coefficient curve of complex surface is shown in Figure 18.

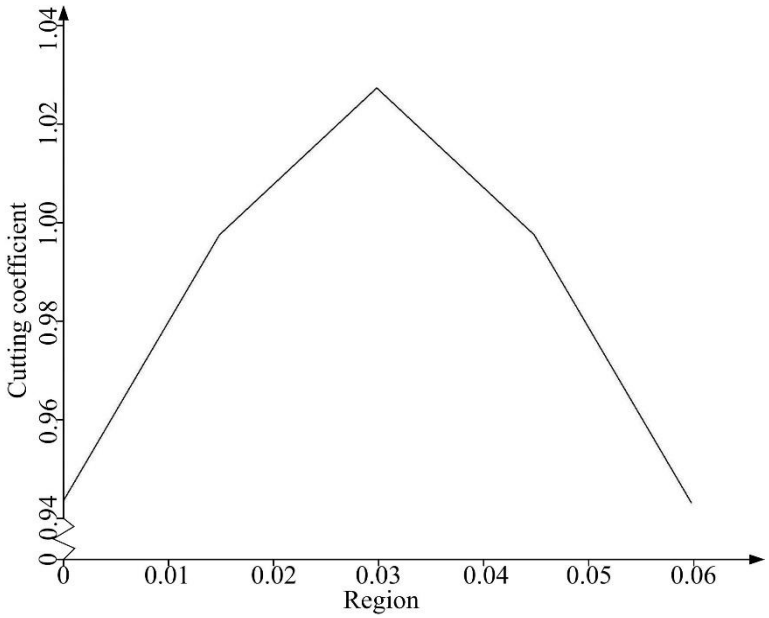

Figure 18. The theoretical cutting coefficient curve of complex surface.

Figure 18 shows that cutting coefficient in L3 is biggest and the theoretical cutting coefficient curve is a line of binary linear equation. When the curvature radius of surface is increased, the cutting coefficient of the surface is closed to the plane. The cutting coefficient of the concave surface is higher than the plane. However, the cutting coefficient of the convex surface is smaller than the plane. The curvature radius of surface is bigger, and the morphology of the concave surface and the convex surface is more closed to the plane. Thus, the cutting coefficient of the concave surface and the convex surface is closed to the plane, with increasing of the curvature radius.

6. Abrasive Flow Processing Experiments and Results Discussion

6.1. Processing Experiment Platform

To check the effectiveness of the improved abrasive flow processing method, a processing experiment platform for complex titanium alloy surfaces of artificial joints was developed, as shown in Figure 19.

(a)

Figure 19. *Cont.*

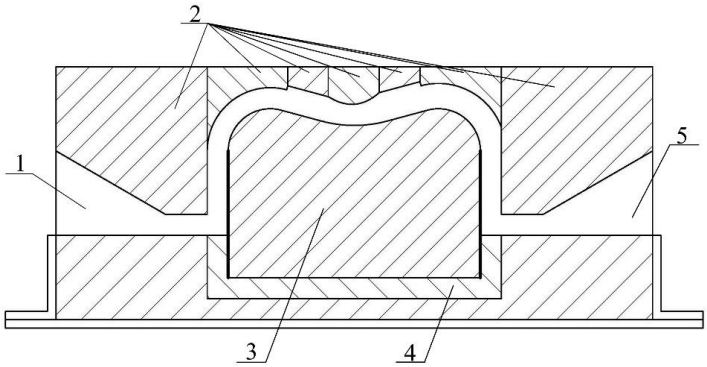

(**b**)

Figure 19. Experimental platform: (**a**) Experiment platform entity: 1, pump; 2, flowmeter; 3, flume; 4, control cabinet; 5, constrained flow passage; 6, experimental table. (**b**) Sectional view of constrained flow passage: 1, inlet; 2, constrained module; 3, workpiece; 4, outlet; 5, fixture.

For the experimental platform, a TC4 titanium alloy workpiece (divided by L1, L2, L3, L4 and L5) was fixed to the base of constrained flow passage, and the multi-segment profiling constrained module was installed on the top of workpiece. The inlet was connected to a high-pressure pump, and the pump was placed in an abrasive flow storage tank. All these devices make up a circular processing system, and the procedures are described as follows: the abrasive flow is pumped from the storage tank by high-pressure pump; the abrasive flow enters the constrained flow passage under a certain high pressure and speed, and forms the fully-developed turbulent state; the workpiece is processed by unordered micro-cutting effects; and, after the abrasive flow finishes cutting work, it will flow back to storage tank with the processed chippings.

There is no nonlinear material removal coefficient in actual processing, so this experiment measures the mass difference of workpiece to validate the influence of curvature in the same conditions of processing equipment, abrasive flow and processing time. The related parameters of processing experiment are shown in Table 2.

Table 2. Processing experiment parameters.

Workpiece Material	Mass Fraction/%	Inlet Velocity/m·s^{-1}	Step	Processing Time/h	Mesh Number
TC4	10	SiC	**1** **2** 3	**1** **2** 3	0.06

6.2. Processing Experiments and Results Discussion

Because the surface appearance of all areas is different, Step 1 is used to eliminate the burrs by rough machining. The surface appearance is observed every 1 h, the material removal amount is measured every 0.5 h after Step 1, and the experimental effect is recorded. As shown in Figure 19, the workpiece has a curvature surface and is divided into five blocks. The workpiece surface quality is measured by the white-light interferometer. The material removal amount is measured by precision electronic scale, and the accuracy of scale is 0.1 mg. The comparative processing experiment results of surface roughness are shown in Figure 20.

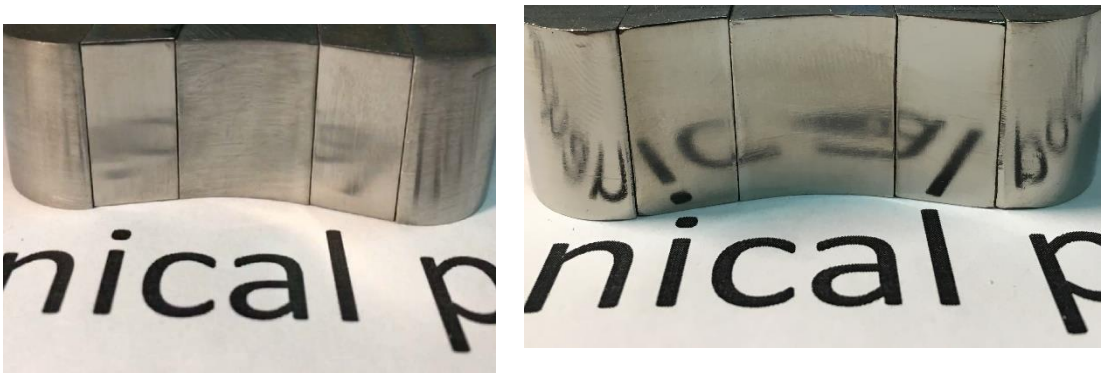

(**a**) (**b**)

Figure 20. Workpiece surface: (**a**) original workpiece; and (**b**) finished workpiece.

Figure 20 shows that the proposed abrasive flow processing method can perform an apparent processing result for the workpiece with complex surface. The surface appearance data of processing experiment are shown in Figures 21–24.

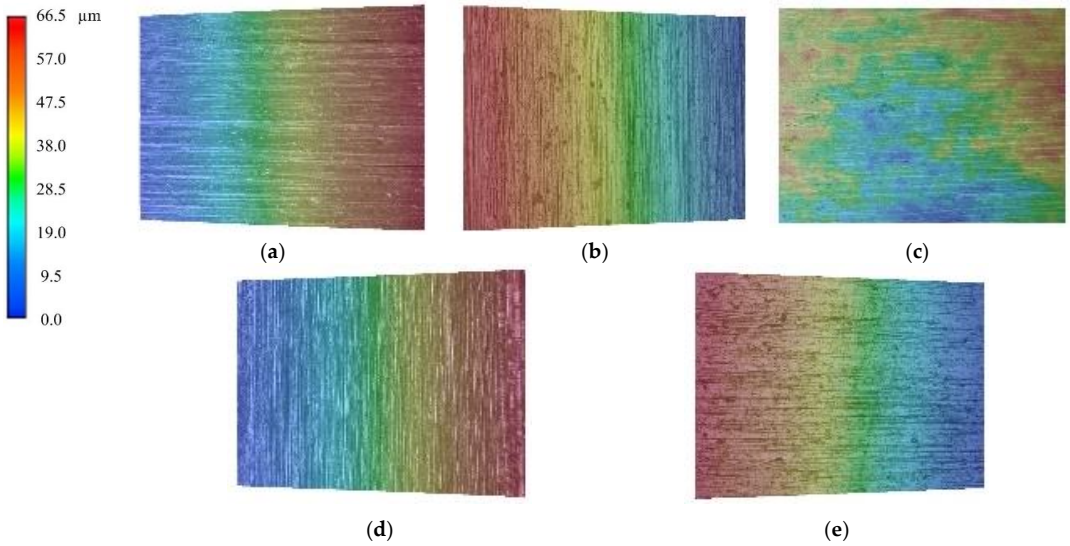

Figure 21. The surface appearance of five regions before processing: (**a**) L1, (**b**) L2, (**c**) L3, (**d**) L4, (**e**) L5.

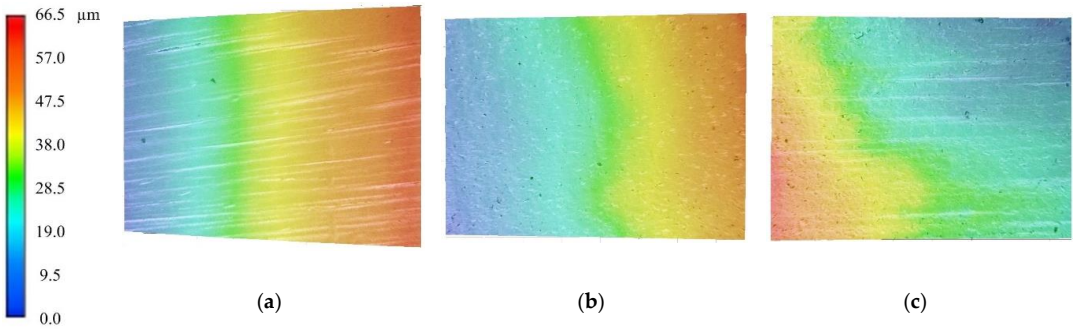

Figure 22. *Cont.*

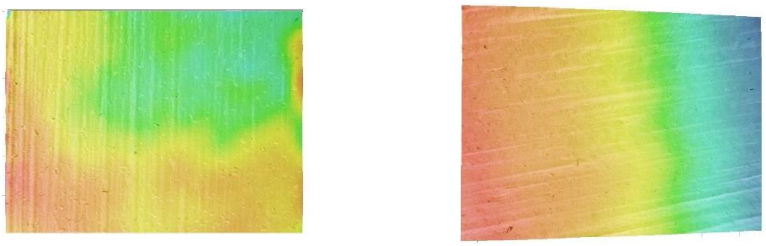

(**d**) (**e**)

Figure 22. The surface appearance of five regions after 1 h processing: (**a**) L1, (**b**) L2, (**c**) L3, (**d**) L4, (**e**) L5.

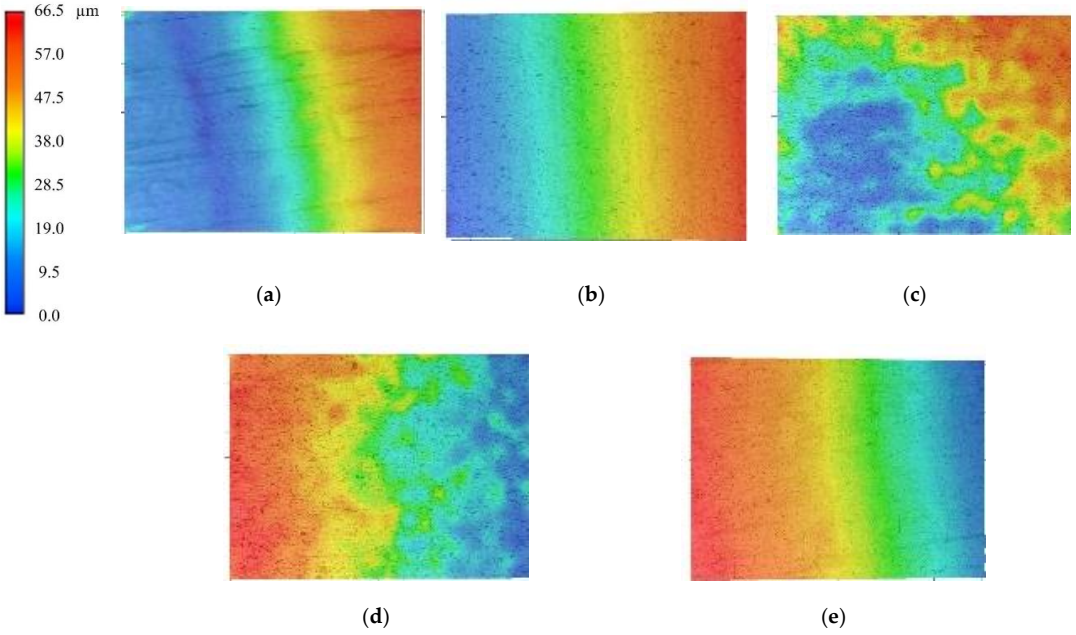

(**a**) (**b**) (**c**)

(**d**) (**e**)

Figure 23. The surface appearance of five regions after 3 h processing: (**a**) L1, (**b**) L2, (**c**) L3, (**d**) L4, (**e**) L5.

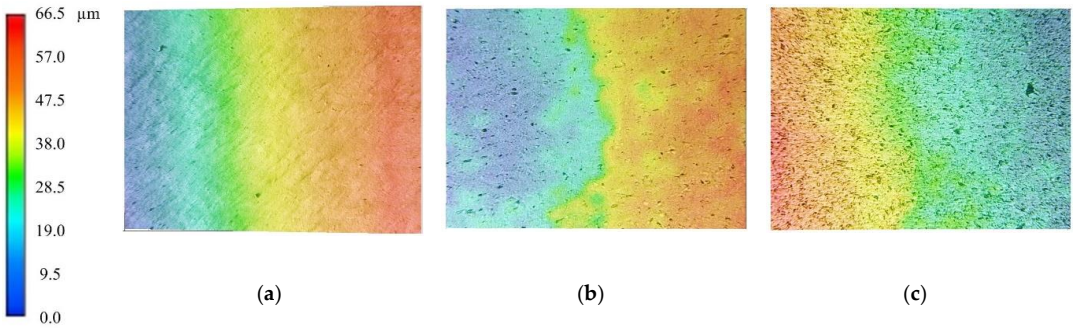

(**a**) (**b**) (**c**)

Figure 24. *Cont.*

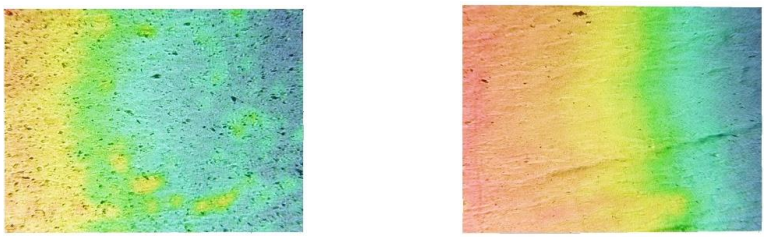

(**d**) (**e**)

Figure 24. The surface appearance of five regions after 5 h processing: (**a**) L1, (**b**) L2, (**c**) L3, (**d**) L4, (**e**) L5.

In Figures 21–24, we can find that the scratches on the workpiece almost disappeared after 3 h, but pits were dug by particles after 3 h. L3 had the most pits, L1 and L5 had the fewest. It is obvious that the concave is more easily processed by particles than the convex.

The workpiece surface roughness is measured by a white-light interferometer, and the results are as shown in Figures 25 and 26. After 5 h, average surface roughness of whole workpiece decreased from 345.74 nm to 56.8 nm, and the surface roughness of best processing area even dropped to 49.46 nm. Many obvious scratches were on the workpiece before processing, while all scratches disappeared after processing. Meanwhile, some pits were made by particles, with even distribution.

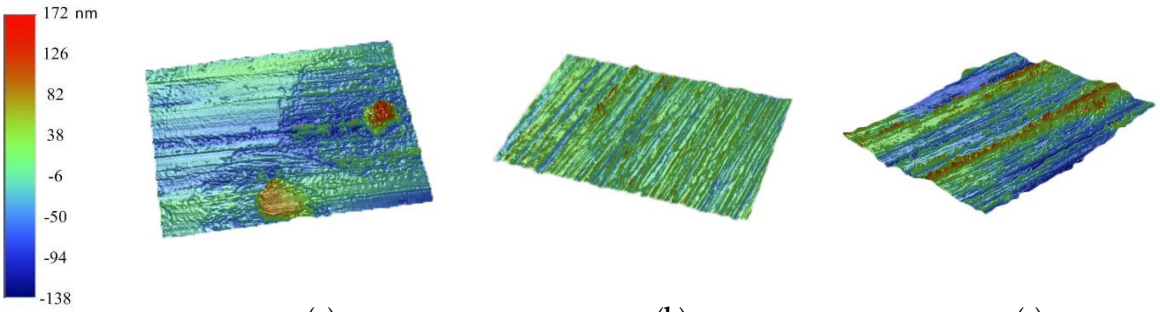

(**a**) (**b**) (**c**)

Figure 25. The surface roughness before processing: (**a**) Ra = 345.74 nm, (**b**) Ra = 203.61 nm, (**c**) Ra = 334.11 nm.

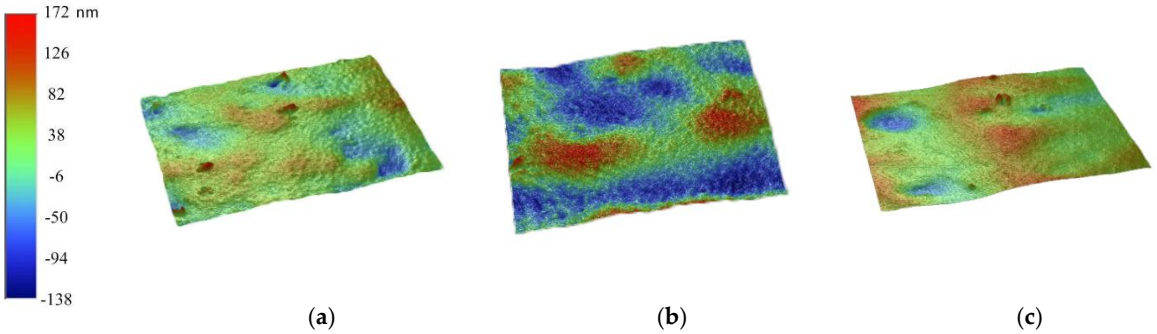

(**a**) (**b**) (**c**)

Figure 26. The surface roughness after processing: (**a**) Ra = 49.46, (**b**) Ra = 66.32, (**c**) Ra = 70.54.

The material removal mass of five blocks are shown in Figure 27. Compared with results of five blocks, the material removal mass increased as the curvature increased. Over time, the material removal mass became smaller. To keep processing efficiency, the processing conditions should be adjusted in the processing. The cutting coefficient K_0 of different positions is shown in Figure 28.

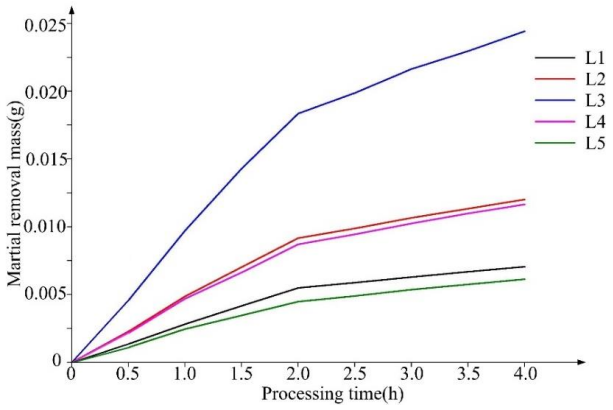

Figure 27. Curve of material removal mass.

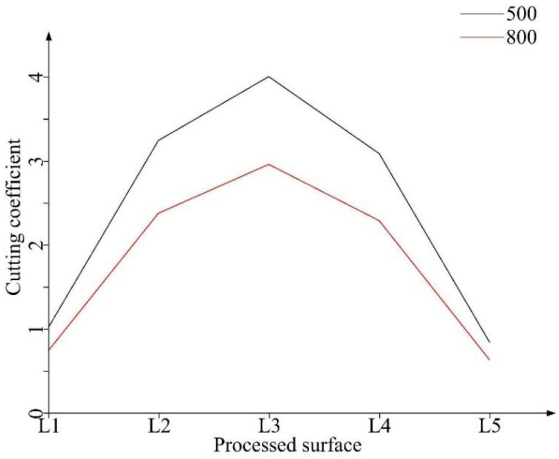

Figure 28. The cutting coefficient K_0 of different position.

The results have shown that the proposed abrasive flow processing method has a good practical processed effect. In addition, the result of this experiment shows that the coefficient of cutting depth of abrasive flow processing is changeable. As the curvature of workpiece increased, K_0 increased. To keep processing efficiency, the hydraulic diameter of the flow passage should be adjusted according to the curvature of workpiece, which can reduce the processing effect differences on the positions with different curvatures.

7. Conclusions

To address the technical problems of precise processing for complex geometric surfaces of titanium alloy artificial joints, this paper sets up a material removal theoretical model of abrasive flow, and proposes an improved abrasive flow processing method. For the above research target, related research works have been performed, and the conclusions are as follows.

(1) A material removal model of abrasive flow is proposed to reveal the processing regularities for complex geometric surfaces of titanium alloy artificial joints. In combination with the realizable k-ε turbulence model, the total force affecting a wall region of constrained flow passage is obtained to estimate the quantity of material removal.

(2) To improve the processing effects, a multi-segment profiling constrained flow passage is designed, and an optimized flow passage scheme is provided according to the surface curvature variation.

(3) Numerical results show that the optimized flow passage can improve the pressure/velocity profile uniformities of abrasive particles. By the product of velocity and pressure, the cutting coefficient

for complex surface is obtained. The cutting coefficient of the concave surface and the convex surface is closed to the plane, with increasing of the curvature radius.

(4) Processing experiment results show that the proposed material removal model is verified by the processing experiment results; the proposed abrasive flow processing method can perform an apparent processing result for the workpiece with complex surface; the scratches on the workpiece almost disappeared after 3 h, but pits were dug by particles after 3 h. As the curvature of workpiece increased, the cutting depth coefficient K_0 increased.

Subsequent research works will be conducted on the facets of processing efficiency optimization, surface biocompatibility of artificial joint and multi-phase abrasive flow processing method.

Author Contributions: L.Z. performed the experiments and wrote the paper; Z.Y. conceived and designed the experiments; D.T. addressed the theoretical modeling and provided technical guidance for this paper; and Y.H. conducted the surface measurement of workpiece samples.

Funding: The authors are grateful for financial support from the following research grants: (1) the Natural Science Foundation of China (grant Nos. 51575493 and 51775501); (2) the Zhejiang Provincial Science Foundation (grant Nos. LY15E050020 and LR16E050001); and (3) the Commonweal Technology Project of Science and Technology Department of Zhejiang Province (grant No. 2012C21093).

Conflicts of Interest: The authors declare no conflict of interest.

References

1. Zhang, L.; Wang, J.S.; Tan, D.P.; Yuan, Z.M. Gas compensation-based abrasive flow processing method for complex titanium alloy surfaces. *Int. J. Adv. Manuf. Technol.* **2017**, *92*, 3385–3397. [CrossRef]
2. Choudhury, D.; Lackner, J.M.; Major, L. Improved wear resistance of functional diamond like carbon coated Ti-6Al-4V alloys in an edge loading conditions. *J. Mech. Behav. Biomed. Mater.* **2016**, *6*, 586–595. [CrossRef] [PubMed]
3. Yi, P.Y.; Peng, L.F.; Huang, J.Q. Multilayered TiAlN films on Ti6Al4V alloy for biomedical applications by closed field unbalanced magnetron sputter ion plating process. *Mater. Sci. Eng. C Mater. Biol. Appl.* **2016**, *2*, 669–676. [CrossRef] [PubMed]
4. Ye, X.X.; Tang, G.Y. Effect of coupling asynchronous acoustoelectric effects on the corrosion behavior, microhardness and biocompatibility of biomedical titanium alloy strips. *J. Mater. Sci. Mater. Med.* **2015**, *26*, 178–188. [CrossRef] [PubMed]
5. Tan, D.P.; Zhang, L.B.; Ai, Q.L. An embedded self-adapting network service framework for networked manufacturing system. *J. Intell. Manuf.* **2016**, in press. [CrossRef]
6. Zhao, Z.F.; Ping, N.; Di, J.; Zheng, H.J. Highly selective adsorption of organic dyes onto tungsten trioxide nanowires. *Res. Chem. Intermed.* **2016**, *42*, 5639–5651. [CrossRef]
7. Zeng, X.; Ji, S.M.; Jin, M.S.; Tan, D.P.; Li, J.H.; Zeng, W.T. Investigation on machining characteristic of pneumatic wheel based on softness consolidation abrasives. *Int. J. Precis. Eng. Manuf.* **2014**, *15*, 2031–2039. [CrossRef]
8. Ji, S.M.; Xiao, F.Q.; Tan, D.P. Analytical method for softness abrasive flow field based on discrete phase model. *Sci. China Technol. Sci.* **2010**, *53*, 2867–2877. [CrossRef]
9. Tan, D.P.; Ji, S.M.; Jin, M.S. Intelligent computer-aided instruction modeling and a method to optimize study strategies for parallel robot instruction. *IEEE Trans. Educ.* **2013**, *56*, 268–273. [CrossRef]
10. Wu, M.G.; Lu, C.D.; Tan, D.P.; Hong, T.; Chen, G.H.; Wen, D.H. Effects of metal buffer layer for amorphous carbon film of 304 stainless steel bipolar plate. *Thin Solid Films* **2016**, *616*, 507–514.
11. Li, J.; Ji, S.M.; Tan, D.P. Improved soft abrasive flow finishing method based on turbulent kinetic energy enhancing. *Chin. J. Mech. Eng.* **2017**, *30*, 301–309. [CrossRef]
12. Li, C.; Ji, S.M.; Tan, D.P. Multiple-loop digital control method for 400Hz inverter system based on phase feedback. *IEEE Ttans. Power Electron.* **2016**, *28*, 408–417. [CrossRef]
13. Tan, D.P.; Chen, S.T.; Bao, G.J.; Zhang, L.B. An embedded lightweight GUI component library and the ergonomics optimization method for industry process monitoring. *Front. Inf. Technol. Electron. Eng.* **2017**, in press. [CrossRef]
14. Ma, B.L.; Ji, S.M.; Tan, D.P. Softness abrasive flow machining. *Adv. Manuf. Technol. Syst.* **2012**, *159*, 262–266.

15. Ge, J.Q.; Tan, D.P.; Ji, S.M. A gas-liquid-solid three-phase abrasive flow processing method based on bubble collapsing. *Int. J. Adv. Manuf. Technol.* **2018**, *95*, 1069–1085. [CrossRef]
16. Tan, D.P.; Ji, S.M.; Li, P.Y.; Pan, X.H. Development of vibration style ladle slag detection method and the key technologies. *Sci. China Technol. Sci.* **2010**, *53*, 2378–2387. [CrossRef]
17. Ji, S.M.; Xiao, F.Q.; Tan, D.P. A new ultraprecision machining method with softness abrasive flow based on discrete phase model. *Adv. Mater. Res.* **2010**, *97–101*, 3055–3059. [CrossRef]
18. Zeng, X.; Ji, S.M.; Tan, D.P.; Jin, M.S.; Wen, D.H.; Zhang, L. Softness consolidation abrasives material removal characteristic oriented to laser hardening surface. *Int. J. Adv. Manuf. Technol.* **2013**, *69*, 2323–2332. [CrossRef]
19. Zhanga, W.Y.; Bapat, S.; Malshe, A.P.; Rajurkar, K.P. Understanding evolution of tribo-chemical interfaces during boundary lubrication in manufacturing. *CIRP Ann. Manuf. Technol.* **2017**, *66*, 555–558. [CrossRef]
20. Rajendra, K.J. Specific energy and temperature determination in abrasive flow machining process. *Int. J. Mach. Tools Manuf.* **2001**, *41*, 1689–1704.
21. Gorana, V.K.; Jain, V.K.; Lal, G.K. Forces prediction during material deformation in abrasive flow machining. *Wear* **2006**, *206*, 128–139. [CrossRef]
22. Yan, M.L.; Li, Y.Z. The experimental study on the abrasive flow machining for gears. *Mod. Manuf. Eng.* **1985**, *1*, 37–39.
23. Wang, W.Y.; Duan, R.H. Study on the principle of viscoelastic abrasive flow machining. *Diam. Abras. Eng.* **1989**, *3*, 17–23.
24. Tang, Y.; Chen, D.Z.; Zhang, F.Y. Effect of pressure parameters of AFM on the machined surface roughness. *J. South China Univ. Technol.* **1997**, *25*, 22–25.
25. Tan, D.P.; Li, P.Y.; Pan, X.H. Application of improved HMM algorithm in slag detection system. *J. Iron Steel Res. Int.* **2009**, *16*, 1–6. [CrossRef]
26. Zhong, M.P.; Yuan, J.L.; Yao, W.F.; Chen, Z.X.; Feng, K.P. Double-curved disc ultrasonic-assisted lapping of precision-machined crowned rollers. *Int. J. Adv. Manuf. Technol.* **2018**, in press. [CrossRef]
27. Tan, D.P.; Yang, T.; Zhao, J.; Ji, S.M. Free sink vortex Ekman suction-extraction evolution mechanism. *ACTA Phys. Sin.* **2016**, *65*, 054701.
28. Zhao, Z.F.; Zhou, H.; Zheng, L.X.; Niu, P.; Yang, G.; Hu, W.W.; Ran, J.R.; Qiao, S.Z.; Wang, J.G.; Zheng, H.J. Molecules interface engineering derived external electric field for effective charge separation in photoelectrocatalysis. *Nano Energy* **2017**, *42*, 90–97. [CrossRef]
29. Li, C.; Ji, S.M.; Tan, D.P. Softness abrasive flow method oriented to tiny scale mold structural surface. *Int. J. Adv. Manuf. Technol.* **2012**, *61*, 975–987. [CrossRef]
30. Lopez, J.; Pineda, H.; Bello, D.; Ratkovich, N. Study of liquid-gas two-phase flow in horizontal pipes using high speed filming and computational fluid dynamics. *Exp. Therm. Fluid Sci.* **2016**, *9*, 126–134. [CrossRef]
31. Ji, S.M.; Weng, X.X.; Tan, D.P. Analytical method of softness abrasive two-phase flow field based on 2D model of LSM. *Acta Phys. Sin.* **2012**, *1*, 188–198.
32. Yuan, Q.; Ji, S.; Wen, D.; Tan, D. Simulation and experiment of soft abrasive flow machining based on improved low-Reynolds-number turbulence model. *China Mech. Eng.* **2014**, *25*, 800–807.
33. Zhang, L.; Deng, B.; Xie, Y.; Zhang, R.; Ji, S.; Wen, D. Curved surface turbulence precision machining method for artificial joint complex of titanium alloy. *Mater. Res. Innov.* **2015**, *19*, 55–59. [CrossRef]
34. Kuncicka, L.; Kocich, R.; Lowe, T.C. Advances in metals and alloys for joint replacement. *Prog. Mater. Sci.* **2017**, *88*, 232–280. [CrossRef]
35. Shih, T.H.; Liou, W.W.; Shabbir, A. A new eddy viscosity model for high Reynolds number turbulent flows. *Comput. Fluids* **1995**, *24*, 227–238. [CrossRef]
36. Tan, D.P.; Li, L.; Zhu, Y.L.; Zheng, S.; Yin, Z.C.; Li, D.F. Critical penetration condition and Ekman suction-extraction mechanism of sink vortex. *J. Zhejiang Univ. Sci. A* **2017**, in press. [CrossRef]
37. Zhang, L.B.; Lv, H.P.; Tan, D.P.; Xu, F.; Chen, J.L.; Bao, G.J.; Cai, S.B. An adaptive quantum genetic algorithm for task sequence planning of complex assembly systems. *Electron. Lett.* **2018**, in press. [CrossRef]
38. Chen, S.T.; Tan, D.P. A SA-ANN-based modeling method for human cognition mechanism and the PSACO cognition algorithm. *Complexity* **2018**, *2018*, 6264124. [CrossRef]
39. Di, J.; Li, Y.; Zhao, Z.F.; Zheng, H.J. A facile synthesis of tungsten carbide/carbon nanocomposite as a non-platinum electrocatalyst for methanol oxidation. *J. Nanosci. Nanotechnol.* **2016**, *16*, 7579–7583. [CrossRef]
40. Nassauer, B.; Hess, A.; Kuna, M. Numerical and experimental investigations of micromechanical processes during wire sawing. *Int. J. Solids Struct.* **2014**, *7*, 2656–2665. [CrossRef]

41. Tan, D.P.; Zhang, L.B. A WP-based nonlinear vibration sensing method for invisible liquid steel slag detection. *Sens. Actuator B Chem.* **2014**, *202*, 1257–1269. [CrossRef]
42. Zheng, H.J.; Niu, P.; Zhao, Z.F. Carbon quantum dot sensitized Pt@Bi_2WO_6/FTO electrodes for enhanced photoelectro-catalytic activity of methanol oxidation. *RSC Adv.* **2017**, *7*, 26943–26951. [CrossRef]
43. Grabon, W.; Pawlus, P.; Wos, S.; Koszela, W.; Wieczorowski, M. Effects of cylinder liner surface topography on friction and wear of liner-ring system at low temperature. *Tribol. Int.* **2018**, *121*, 148–160. [CrossRef]
44. Jain, V.K. Magnetic field assisted abrasive based micro-/nano-finishing. *J. Mater. Process. Technol.* **2009**, *209*, 6022–6038. [CrossRef]
45. Tan, D.; Li, P.; Pan, X. Intelligent industry monitoring network architecture UPnP based. *Chin. J. Electron.* **2008**, *17*, 607–610.
46. Haan, J.J.; Steif, P.S. Abrasive wear due to the slow flow of a concentrated suspension. *Wear* **1998**, *219*, 177–183. [CrossRef]
47. Song, R.; Chen, S.T. A self-tuning proportional-integral-derivative-based temperature control method for draw-texturing-yarn machine. *Math. Probl. Eng.* **2017**, *2017*, 1864321. [CrossRef]
48. Tan, D.P.; Li, P.Y.; Ji, Y.X.; Wen, D.H.; Li, C. SA-ANN-based slag carry-over detection method and the embedded WME platform. *IEEE Trans. Ind. Electron.* **2013**, *60*, 4702–4713. [CrossRef]
49. Wang, G.L.; Wang, Y.Q.; Xu, Z.X. Modeling and analysis of the material removal depth for stone polishing. *J. Mater. Process. Technol.* **2009**, *209*, 2453–2463. [CrossRef]
50. Di, J.; Fu, X.C.; Zheng, H.J.; Jia, Y. H-TiO_2/C/MnO_2 nanocomposite materials for high-performance supercapacitors. *J. Nanopart. Res.* **2015**, *17*, 225. [CrossRef]
51. Wang, G.L.; Zhou, X.Q.; Yang, X.; Zhou, H.B.; Chen, G.J. Material removal profile for large mould polishing with coated abrasives. *Int. J. Adv. Manuf. Technol.* **2015**, *80*, 625–635. [CrossRef]
52. Li, Y.B.; Tan, D.P.; Wen, D.H.; Ji, S.M.; Cai, D.H. Parameters optimization of a novel 5-DOF gasbag polishing machine tool. *Chin. J. Mech. Eng.* **2013**, *26*, 680–688. [CrossRef]
53. Tan, D.P.; Li, L.; Zhu, Y.L.; Zheng, S.; Ruan, H.J.; Jiang, X.Y. An embedded cloud database service method for distributed industry monitoring. *IEEE Trans. Ind. Inform.* **2017**, in press. [CrossRef]
54. Atkins, A.G.; Liu, J.H. Toughness and the transition between cutting and rubbing in abrasive contacts. *Wear* **2007**, *262*, 146–159. [CrossRef]
55. Zeng, X.; Ji, S.M.; Jin, M.S.; Tan, D.P.; Ge, J.Q. Research on dynamic characteristic of softness consolidation abrasives in machining process. *Int. J. Adv. Manuf. Technol.* **2016**, *82*, 1115–1125. [CrossRef]
56. Guo, H.; Li, J.Y.; Ma, T.F. 3-D numerical simulation on micro-hole of the common-rail pipe abrasive flow machining. In *Applied Mechanics and Materials*; Trans Tech Publications: Princeton, NJ, USA, 2013; pp. 202–206.
57. Ji, S.M.; Ma, B.L.; Tan, D.P. The numerical simulation of the single abrasive motion law in the environment of structural surface. In *Applied Mechanics and Materials*; Trans Tech Publications: Princeton, NJ, USA, 2010; pp. 573–577.
58. Wang, M.B.; Wang, R.H. Euler/Euler theory and application of fluid-particle two-phase jet. *J. Hydrodyn.* **2006**, *7*, 120–124. [CrossRef]
59. Tan, D.P.; Ji, S.M.; Fu, Y.Z. An improved soft abrasive flow finishing method based on fluid collision theory. *Int. J. Adv. Manuf. Technol.* **2016**, *85*, 1261–1274. [CrossRef]
60. Ji, S.M.; Ge, J.Q.; Tan, D.P. Wall contact effects of particle-wall collision process in two-phase particle fluid. *J. Zhejiang Univ. Sci. A* **2017**, *18*, 958–973. [CrossRef]
61. Tan, D.P.; Ni, Y.S.; Zhang, L.B. Two-phase sink vortex suction mechanism and penetration dynamic characteristics in ladle teeming process. *J. Iron Steel Res. Int.* **2017**, *24*, 669–677. [CrossRef]
62. Chen, J.L.; Xu, F.; Tan, D.P.; Shen, Z.; Zhang, L.B.; Ai, Q.L. A control method for agricultural greenhouses heating based on computational fluid dynamics and energy prediction model. *Appl. Energy* **2015**, *141*, 106–118. [CrossRef]
63. Zhang, L.; Yuan, Z.; Qi, Z.; Cai, D.; Cheng, Z.; Qi, H. CFD-based study of the abrasive flow characteristics within constrained flow passage in polishing of complex titanium alloy surfaces. *Powder Technol.* **2018**, *333*, 209–218. [CrossRef]